

Practical High-Fidelity Novel-View Synthesis of Mounted Lepidoptera

Kristof Overdulve Lode Jorissen Nick Michiels
 Digital Future Lab, Flanders Make, Hasselt University
 {kristof.overdulve, lode.jorissen, nick.michiels}@uhasselt.be



Figure 1. **Photo-realistic 3D reconstruction of mounted Lepidoptera.** We present a pipeline for the photo-realistic 3D reconstruction of mounted Lepidoptera. This is challenging as such specimens are typically small, necessitating the use of macro lenses with a severely limited depth of field (DoF), and a conventional camera cannot reach the ventral side without physically moving the fragile specimen. Our pipeline combines handheld focus stacking and a non-contact mirror system to overcome these challenges, yielding a single consistent model that can be rendered from any viewpoint.

Abstract

Mounted butterflies are among the most striking objects in natural history collections. However, their beauty is notoriously hard to digitize in 3D: they are small and fragile, with microscopic hairs and vein structures. Capturing them in sufficient detail, therefore, requires a macro lens, which has a very limited Depth of Field (DoF). Moreover, a camera body cannot be maneuvered beneath a pinned specimen to photograph its ventral surface (the underside of the wings). We introduce an end-to-end pipeline that resolves these challenges to turn such specimens into photo-realistic 3D models viewable from every direction. It combines three ingredients: handheld focus stacking for all-in-focus macro capture without a tripod, a non-contact first-surface mirror system that exposes the ventral surface without touching the

specimen, and a segmentation-free, mirror-aware 3D Gaussian Splatting extension. We validate the reconstructions on four diverse specimens.

1. Introduction

Natural history collections worldwide hold tens of millions of pinned insect specimens, representing an irreplaceable record of biodiversity accumulated over centuries. Lepidoptera (butterflies and moths) form one of the largest and most visually studied groups, prized scientifically and aesthetically for the iridescent scales and patterns covering their wings. Digitizing these collections for virtual museums, educational platforms, and open-access scientific repositories is an active priority, reflected in initiatives such as iDigBio, DiSSCo [16], and SYNTHESYS+ [24].

However, existing scanning workflows are designed for flat herbarium sheets or robust three-dimensional objects that can be moved for professional imaging.

Mounted butterflies fall into a uniquely challenging middle ground. Firstly, macro-lens photography is required to capture the fine-scale microstructures (microscopic hairs, scale rows, wing veins, and the iridescent nanostructures) in sufficient resolution, as they carry significant scientific and aesthetic value. Such macro lenses, however, have a depth-of-field (DoF) of only a few millimeters, so most of the specimen is out of focus in a single shot. Secondly, a large mirrorless camera body cannot be maneuvered beneath a pinned butterfly to photograph the ventral surface (the underside of its wings). Removing a specimen from its case to hang it freely on nylon monofilament—standard practice for more robust insects such as beetles—risks irreparable damage as mounted Lepidoptera are extraordinarily fragile. Curators describe handling mounted butterflies as working with “dust”. Synthetically mirroring the dorsal (upper) surface to stand in for the ventral surface is not a viable shortcut: in many species, the dorsal and ventral wing patterns differ entirely, so the true ventral surface must be imaged directly.

We address these challenges with a single, reproducible *methodology* that combines established techniques into a workflow tailored to the reconstruction of mounted Lepidoptera (Fig. 2). Our contributions are:

- A **non-contact, segmentation-free mirror approach** for imaging the ventral surface of Lepidoptera through first-surface mirrors (Sec. 3.1) and a mirror-aware extension of 3DGS (Sec. 3.3) to reconstruct a single, consistent specimen without the need for per-pixel segmentation masks.
- A **handheld focus stacking pipeline** with automatic image registration (Sec. 3.2) that produces all-in-focus images from a handheld mirrorless camera equipped with a macro lens, eliminating the need for tripods or motorized focus rails.

Together, these components form a practical end-to-end pipeline that turns a fragile, pinned butterfly into a photorealistic 3D model viewable from any direction.

2. Related Work

2.1. Heritage and specimen digitization

Early work on 3D insect digitization relied on classical reconstruction methods such as visual hulls, which struggle with concavities, fine structures, and view-dependent appearance [17] and thus lack photorealism. Later systems improved acquisition by using calibrated extended-depth-of-field imaging [9, 29] and automated hardware setups [18, 25]. Although effective, these systems are expensive and difficult to move.

2.2. Novel-View Synthesis

NeRF [13] has transformed the field of novel-view synthesis (NVS) and 3D reconstruction. It represents a scene as a continuous volumetric function optimized by differentiable ray marching through a Multi-Layer Perceptron (MLP). While NeRF achieves photorealistic quality, models fine structures, and reproduces view-dependent appearance, its implicit nature results in slow training and rendering, prohibiting real-time applications. Subsequent approaches aimed at accelerating NeRF by using voxel grids [6] or multi-resolution hash encodings [14]. Most notably, Kerbl et al. introduced 3D Gaussian Splatting (3DGS) [8], representing the scene as a set of anisotropic 3D Gaussians rasterized onto the image plane, combining state-of-the-art quality with real-time performance.

As radiance-field representations excel at modeling fine structures and view-dependent effects, they are uniquely suited for 3D digitization of insects. They can capture microscopic hairs and, in the case of butterflies, reproduce the strongly angle-dependent iridescent colors of their scales. As a result, neural methods have been explored for insect reconstruction. Xu et al. evaluated learning-based reconstruction, including NeRF-style methods, under insect-specific failure modes such as thin structures, specular cuticle, and translucent wings [29]. Amrani et al. adapted neural implicit surfaces to better preserve fine insect detail, especially wing venation and antennae, through detail-aware sampling [1]. Existing work, however, leaves a gap in 3D digitization of Lepidoptera, as their long shape exacerbates macro defocus issues and poses challenges for reconstructing the ventral surface, which is difficult to observe when mounted.

Depth of field and defocus in 3D reconstruction. Most novel-view-synthesis methods assume a pinhole camera and all-in-focus inputs. A promising line of work aims to model finite-aperture lenses more accurately to recover a sharp scene from defocus-degraded captures. In the NeRF literature, Deblur-NeRF [11] learns per-ray blur kernels end-to-end. For 3DGS, DOF-GS [27] and DoF-Gaussian [23] introduce explicit thin-lens/finite-aperture camera models with a differentiable circle-of-confusion to recover a sharp 3D scene from multi-view images containing defocus blur. However, they target ordinary-scale photography with *moderate* defocus, where each image still contains a largely recoverable sharp signal, and the reconstruction must disambiguate blur from geometry, an inherently ill-posed inverse problem.

Focus stacking. Focus stacking composites a sequence of images, each focused at a different depth, into a single all-in-focus result; methods differ in sharpness estimation (gradient energy [15], Laplacian variance, wavelet coefficients)

and fusion strategy, and commercial tools (Helicon Focus, Zerene Stacker) are widely used in scientific macro photography. Standard focus stacking, however, assumes static, tripod-mounted capture, which is inconvenient when many viewpoints need to be imaged. Our system instead performs per-stack image registration to compensate for hand jitter before fusion (Sec. 3.2), enabling handheld use. We show in Sec. 4.3 that, in the extreme macro regime of mounted Lepidoptera, this acquire-then-fuse strategy clearly outperforms DoF-aware 3DGS methods.

Mirror and reflection handling. Without explicit handling, mirror-like reflections cause a radiance field to reconstruct the reflected content as if it were real geometry behind the mirror surface. MirrorGaussian [10] and Mirror-3DGS [12], similar to our method, explicitly deal with the presence of mirrors by either rendering the virtual image by reflecting the real 3D Gaussians across a 3D plane [10] or by rendering a second image from a mirrored camera viewpoint [12]. Both methods require a *per-image mirror-segmentation mask* to supervise the mirror-plane parameters during training. Our approach, instead, is *segmentation-free*: we recover the mirror plane geometrically from the bilateral symmetry of the dense point cloud (Sec. 3.3.2) obtained through Multi-view Stereo and reflect the *entire* Gaussian set across it (Sec. 3.3.3). This is possible for our use case, as we are not interested in the scene content on the other side of the mirror plane.

3. Method

Figure 2 gives an overview of the pipeline. A photographer acquires N focus stacks from different viewpoints $\omega_1, \dots, \omega_N$ using a mirrorless camera with a macro lens. First-surface mirrors are positioned to expose the ventral surface. Each stack of K images is registered and merged into one all-in-focus image. From the resulting image collection, we estimate camera poses with HLOC [20] using SuperGlue features [21] and recover a *dense* point cloud by COLMAP multi-view stereo [22] (per-view dense stereo estimation followed by depth-map fusion). This dense point cloud—rather than the much sparser structure-from-motion keypoints—both initializes the Gaussians and is used to detect the mirror plane. The images, poses, and dense point cloud are fed into our mirror-aware 3DGS, yielding a single, consistent digital 3D representation that supports real-time rendering.

3.1. Non-Contact Mirror System

A mounted butterfly rests with one side up (typically its dorsal side) on a spreading board with its pin driven through the thorax, leaving the ventral surface only a pin’s height above the case floor and unreachable by high-quality cameras. Removing the specimen to image it from below is inadvisable

as the wing-to-thorax attachment is held only by dried soft tissue and is easily damaged.

We therefore expose the ventral surface with two *first-surface mirrors* placed around the pin. Unlike ordinary second-surface mirrors, first-surface mirrors have the reflective coating on the front face, so light never passes through the glass. This avoids the faint ghost reflections and color fringing that an ordinary mirror would show. We used inexpensive dental examination mirrors well-suited to the ~ 5 –10 cm scale of mounted specimens. The mirrors lie symmetrically on either side of the specimen on the foam substrate, contacting neither the butterfly nor its pin.

3.2. Handheld Focus Stacking

3.2.1. Capture Protocol

Images are captured with a Canon EOS R5C mirrorless camera fitted with a macro lens. At each viewpoint, we acquire a burst of $K = 20$ frames at continuous drive speed, initially focusing on the nearest part of the specimen. Each frame captures a different depth slice of the butterfly in sharp focus (Figs. 3a and 3b). Because the camera is handheld, consecutive frames exhibit small shifts and rotations due to hand jitter. If uncorrected, these two effects combine to produce ghosting and double-edge smearing artifacts in the fused output (Fig. 3c).

3.2.2. Image Registration

We align the K frames of each stack with the Enhanced Correlation Coefficient (ECC) algorithm of Evangelidis and Psarakis [4], which directly maximizes the correlation between a reference image and a warped source image in pixel space, without needing feature detection or outlier rejection. As ECC operates on single-channel images, we compute a specimen-adaptive projection onto grayscale using Principal Component Analysis (PCA) of the pixel values in the first frame. The first eigenvector of the 3×3 RGB covariance matrix defines the direction of maximum variance in color space. Therefore, projecting each frame onto this axis produces a grayscale image that optimally preserves the image’s contrast.

We then align frames sequentially. For each consecutive pair, we estimate a 2D affine transform $\mathbf{A} \in \mathbb{R}^{2 \times 3}$ (6 degrees of freedom: rotation, translation, anisotropic scale, and shear) by maximizing the ECC criterion:

$$\hat{\mathbf{A}} = \arg \max_{\mathbf{A}} \frac{\langle \tilde{T}, \tilde{I} \circ \mathcal{W}(\cdot; \mathbf{A}) \rangle}{\|\tilde{T}\| \|\tilde{I} \circ \mathcal{W}(\cdot; \mathbf{A})\|}, \quad (1)$$

where T is the reference (already-aligned) frame, I is the source frame, $\mathcal{W}(\cdot; \mathbf{A})$ denotes the affine warp, and $\tilde{\cdot}$ denotes mean-subtraction. We deliberately use an affine model rather than a full projective homography because the camera movement and thus parallax between consecutive

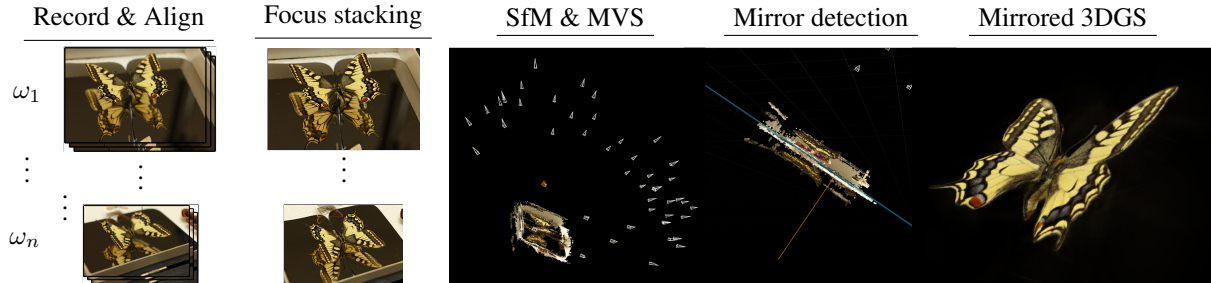


Figure 2. **Pipeline overview.** First-surface mirrors are positioned around the mounted specimen without touching it, and a handheld focus stack is acquired at each viewpoint and registered into an all-in-focus image. Structure-from-motion and multi-view stereo then recover the camera poses and a dense point cloud, from which we detect the mirror plane. Finally, our mirror-aware 3DGS reflects the Gaussians across this plane to learn a single, consistent 3D representation of the specimen for real-time novel-view rendering.

frames is limited. Optimization runs for up to 50 Gauss–Newton iterations with early stopping at a parameter update norm of 10^{-3} .

3.2.3. Multi-Resolution Pyramid Fusion

After alignment, the K registered frames are merged into a single all-in-focus image using Helicon Focus [7] through *pyramid stacking* method. Pyramid stacking is a multi-resolution image fusion technique inspired by Laplacian pyramid blending [2]. The procedure operates as follows. First, a Laplacian pyramid is constructed for each aligned frame by iteratively low-pass filtering and downsampling to form a Gaussian pyramid, then taking the difference between successive levels to isolate band-limited detail at each scale. Then, at each pyramid level and spatial location, a local sharpness weight is computed for each frame, measuring the energy of the band-pass detail signal within a small neighborhood. The level-wise composite is formed by a weighted blend using these sharpness weights, selecting detail from whichever source frame is sharpest at that scale and location. Finally, the composite pyramid is collapsed by iterative upsampling and summation to recover the full-resolution all-in-focus image.

3.3. Segmentation-Free Mirror-Aware 3DGS

3.3.1. Background: 3D Gaussian Splatting

3DGS [8] represents a scene as N anisotropic 3D Gaussians $\{\mathcal{G}_i\}_{i=1}^N$, each parameterized by a mean position $\mu_i \in \mathbb{R}^3$, a covariance Σ_i stored as a scale vector \mathbf{s}_i and unit quaternion \mathbf{q}_i , an opacity α_i , and view-dependent color encoded as spherical harmonic (SH) coefficients. Given a camera viewpoint, Gaussians are projected to 2D, sorted by depth, and alpha-composited front-to-back. The representation is photometrically optimized against the GT image.

3.3.2. Mirror Plane Detection

When a mirror is in the scene, the camera sees the real geometry directly and a reflected image of that *same* geom-

etry in the mirror. None of Structure-from-Motion, Multi-View Stereo, or 3DGS can visually distinguish direct from reflected feature tracks. Without modification, they therefore reconstruct both the direct and the reflected content as real 3D points, producing duplicated geometry and spurious floaters on the unobserved sides of the specimen. Our mirror plane detection exploits the double geometry from SfM+MVS, as it, when a mirror is present, exhibits a distinctive *approximate bilateral symmetry* in its dense point cloud, enabling the computation of plane parameters without user-provided segmentation. We work on the *dense* multi-view-stereo point cloud rather than the sparse structure-from-motion keypoints, because its higher density gives more reliable local geometric descriptors. The mirror plane detection operates through the following steps:

Step 1: Artificial self-mirror. We create an artificial mirror clone \mathcal{P}' of the dense point cloud \mathcal{P} by reflecting all points and normals across the world coordinate X -axis:

$$\mathbf{p}' = \mathbf{M}_X \mathbf{p}, \quad \mathbf{M}_X = \text{diag}(-1, 1, 1). \quad (2)$$

After this flip, the bilateral symmetry of the scene means that \mathcal{P}' and \mathcal{P} are related by a rigid registration that recovers the true mirror plane geometry.

Step 2: FPFH feature extraction. Both clouds are voxel-downsampled at spacing δ ($\delta = 0.01$) and described by Fast Point Feature Histograms (FPFH) [19], 33-dimensional local geometric descriptors computed at radius 5δ .

Step 3: RANSAC global registration. We run feature-matching RANSAC [5] between $\mathcal{P}'_{\text{down}}$ and $\mathcal{P}_{\text{down}}$ with distance threshold 1.5δ , correspondence checkers for edge length (ratio 0.9) and point-to-point distance, and up to 10^5 iterations at 99.9% confidence. The output is a coarse rigid transform $\mathbf{T}_{\text{ransac}} \in SE(3)$ that maps the artificial clone back toward the original.

Step 4: Point-to-Plane ICP refinement. We refine $\mathbf{T}_{\text{ransac}}$ using Point-to-Plane ICP [3] at a tighter threshold 0.4δ , running for up to 100 iterations. Point-to-Plane ICP minimizes the sum of squared distances from each source point to the

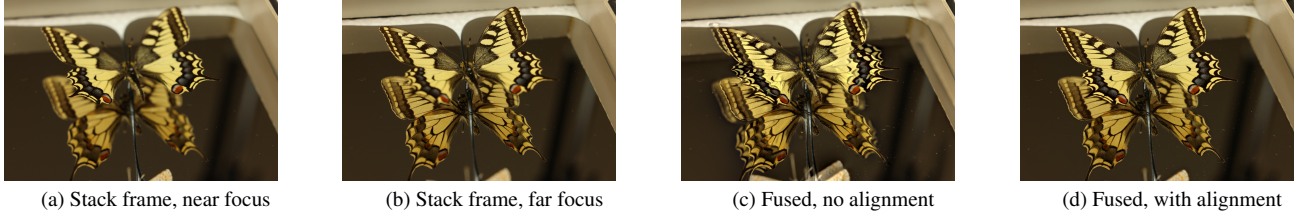


Figure 3. **Handheld focus stacking.** (a, b) show 2 limited DoF depth slices. Pyramid fusion without prior alignment (c) produces ghost edges and scale smearing from handheld jitter. Our ECC-based sequential registration step corrects these misalignments before fusion, yielding a sharp, all-in-focus composite (d).

tangent plane of its target correspondence, which is more accurate than Point-to-Point ICP on curved surfaces such as wing membranes.

Step 5: Plane parameter extraction. The refined transform \mathbf{T}_{icp} maps \mathcal{P}' back to \mathcal{P} , so the composite transformation

$$\mathbf{S} = \mathbf{T}_{\text{icp}} \mathbf{M}_X \quad (3)$$

is itself a reflection across the recovered mirror plane. A 3×3 reflection matrix has eigenvalues $\{+1, +1, -1\}$; the eigenvector corresponding to -1 is the mirror plane normal \mathbf{n} . Denoting the translation part of \mathbf{S} as \mathbf{t}_s , the plane offset is recovered as $d = -\mathbf{n}^\top(\mathbf{t}_s/2)$, since the midpoint $\mathbf{t}_s/2$ lies on the mirror plane by construction. The full plane is therefore

$$\begin{aligned} \mathbf{n}^\top \mathbf{x} + d &= 0, & \mathbf{n} &= \text{eigvec}(\mathbf{S}_{3 \times 3}, \lambda=-1), \\ d &= -\mathbf{n}^\top \frac{\mathbf{t}_s}{2}. \end{aligned} \quad (4)$$

3.3.3. Gaussian Reflection

Given the mirror plane (\mathbf{n}, d) , we extend 3DGS to explain mirror observations without any segmentation mask by reflecting all Gaussians across the plane and concatenating the reflected copies with the originals. The combined $2N$ -Gaussian set is then rasterized from each real training camera, so that direct and mirror-mediated observations are explained simultaneously.

Reflecting Gaussian means. The signed distance of μ_i to the plane is $D_i = \mathbf{n}^\top \mu_i + d$. The reflected position is

$$\mu'_i = \mu_i - 2D_i \mathbf{n}. \quad (5)$$

Reflecting Gaussian orientations. Each Gaussian’s orientation is stored as a unit quaternion \mathbf{q}_i , which we convert to a rotation matrix $\mathbf{R}_i \in SO(3)$. The householder reflection matrix $\mathbf{M} = \mathbf{I} - 2\mathbf{n}\mathbf{n}^\top$ is an improper rotation ($\det(\mathbf{M}) = -1$), so the direct product $\mathbf{M}\mathbf{R}_i$ has determinant -1 and is not a valid rotation. We fix this by negating the first column of the product, which corresponds to flipping the Gaussian’s local x -axis and restores the determinant to $+1$:

$$\tilde{\mathbf{R}}_i = \mathbf{M}\mathbf{R}_i, \quad \mathbf{R}'_i = \tilde{\mathbf{R}}_i \cdot \text{diag}(-1, 1, 1), \quad (6)$$

which is then converted back to a unit quaternion \mathbf{q}'_i via the standard rotation-matrix-to-quaternion formula. Scales s_i , opacities α_i , and SH color coefficients are copied unchanged, as they are properties of the Gaussian in its own local frame and are therefore invariant to the mirror reflection of that frame’s position and orientation.

Combined render. At each training step, before rasterization, we evaluate Eqs. (5) and (6) for all N Gaussians and concatenate:

$$\mathcal{G}_{\text{combined}} = \{\mathcal{G}_i\}_{i=1}^N \cup \{\mathcal{G}'_i\}_{i=1}^N. \quad (7)$$

Standard 3DGS rasterization then renders $\mathcal{G}_{\text{combined}}$ from each real camera. Cameras facing the real scene see the original N Gaussians in the foreground, and the reflected copies behind them (occluded or transparent); cameras facing the mirror see the reflected copies at exactly the positions where the mirror image of the butterfly appears.

3.3.4. Implementation

We build on **LichtFeld-Studio** [26], an open-source native trainer and viewer for 3D Gaussian Splatting, in preference to the reference 3DGS implementation [8] due to its fast training speed, its increasing popularity outside of academic research, and as their *MRNF* refinement strategy, an edge-guided variant of adaptive density control that biases grow-and-split toward image-edge regions and prunes by raw opacity and scale thresholds, preserving fine wing-scale and venation structure noticeably better than reference 3DGS in early experiments. Our segmentation-free mirror reflection is implemented as a Python plugin to LichtFeld-Studio. At each training iteration, the plugin’s pre-rasterize callback evaluates Eqs. (5) and (6) on the current Gaussians under PyTorch autograd and exposes the reflected set as auxiliary splats; the trainer then rasterizes the union of original and auxiliary splats in a single pass. After the backward pass, the plugin folds gradients from the auxiliary splats back onto their source Gaussians through autograd, so the optimizer always operates on a single, consistent Gaussian set. The reflection itself is deterministic and parameter-free, introducing no extra trainable weights. The dense MVS cloud used to initialize the Gaussians is also pre-folded across the



Figure 4. **Evaluation dataset.** The mounted butterfly specimens used for quantitative evaluation were selected for their visual diversity and, in particular, their range of physical sizes.

detected plane onto the camera side for initializing the splats before starting training.

4. Experiments

No prior end-to-end system targets the exact task explored in our paper, so there is no complete system to benchmark against. We therefore organize the evaluation around the key design decisions:

1. **How to handle macro defocus** (Sec. 4.3): all-in-focus *handheld focus stacking* (ours) versus a *depth-of-field-aware 3DGS* that models lens bokeh during training.
2. **How to handle the mirror** (Sec. 4.4): segmentation-free mirror-aware 3DGS versus baseline 3DGS.

4.1. Dataset

We evaluate on **four mounted butterfly specimens**, chosen to span a wide diversity of iridescent color effects, physical sizes, dorsal and ventral wing patterns, and mounting types. For each specimen, we acquire 40–70 focus-stacked view-points (with mirrors). Images are captured at 8K resolution and then downsampled to 4K for novel-view synthesis training.

4.2. Evaluation protocol

We report PSNR, SSIM [28], and LPIPS [30] on held-out views. Because the captured viewpoints per specimen are relatively sparse, we do not rely on the 7/8 for training and 1/8 for testing split common in the NVS literature. Instead, for each specimen we train 7 separate models, each holding out a single, randomly chosen view as its test image, and report the mean over these 7 held-out views (and over specimens). The studies differ in the region scored: the macro-defocus comparison (Sec. 4.3) is evaluated on the *full* image, whereas the mirror comparison (Sec. 4.4) is evaluated on the *manually segmented specimen foreground*, so that

Table 1. **Macro-defocus handling.** Novel-view-synthesis quality of handheld focus stacking (ours) versus depth-of-field-aware 3DGS, averaged over the per-specimen held-out evaluation of Sec. 4.2. Each method is scored on the full image.

Method	PSNR \uparrow	SSIM \uparrow	LPIPS \downarrow
DoF-aware 3DGS [27]	14.679	0.627	0.502
Focus stacking	20.103	0.776	0.230

only the reconstructed butterfly is measured. This masking applies only to the metrics; every qualitative render we show (Figs. 5 and 6) is the raw, full-image output of each method, with no background removal, cleanup, or segmentation.

4.3. Handling macro defocus

Two strategies to address limited DoF captures are available: performing handheld focus stacking before NVS training or using a *depth-of-field-aware 3DGS* [27] on raw shallow-DoF frames. We compare the quality of novel-view synthesis for these two strategies.

Table 1 reports the quantitative comparison and Fig. 5 the qualitative one. On our macro data, DoF-aware 3DGS remains markedly blurry and never recovers the high-frequency scale and vein detail, whereas focus stacking consistently delivers sharp, all-in-focus renders.

4.4. Mirror-aware reconstruction

We compare the quality of novel-view synthesis on held-out test views for our mirror-aware 3DGS extension against baseline 3DGS qualitatively Fig. 6 and quantitatively Tab. 2. A natural extra baseline would be to train a standard, mirror-unaware 3DGS model and fold the Gaussians from the reflected half-space onto the real specimen after training using the detected mirror plane. The results, however, were very poor, as the reflected half-space is so densely populated with spurious background floaters that folding it onto the “real” specimen overwhelms the reconstruction with artifacts. We therefore exclude it from the comparison.

It is important to note that the goal of our quantitative evaluation is, perhaps surprisingly, *not* to report improved image-quality metrics compared to baseline 3DGS on image-quality metrics; the task our method solves is, in fact, strictly harder. Given that we have no ground-truth photographs of the ventral surface, it is observable only as a reflection so every held-out test view is a dorsal-side image that shows the specimen together with its mirror image. A mirror-unaware baseline is free to explain such a view as two independent 3D objects: the directly observed dorsal surface, and a wholly separate “virtual” butterfly behind the mirror that absorbs the reflected ventral surface. It can fit each to the training images independently, without requir-



Figure 5. **Qualitative comparison of macro-defocus handling.** Each column is a held-out view (six views spanning four specimens); the rows show, top to bottom, the ground truth, handheld focus stacking (ours), and DoF-aware 3DGS [27].

Table 2. **Mirror-aware reconstruction.** Novel-view-synthesis quality on held-out views, averaged over the per-specimen held-out evaluation of Sec. 4.2. The aim is not to surpass the mirror-unaware baseline but to show that enforcing a single, physically consistent butterfly does not meaningfully degrade novel-view quality relative to the less-constrained baseline.

Method	PSNR \uparrow	SSIM \uparrow	LPIPS \downarrow
No mirroring	23.75	0.731	0.0546
Ours	23.51	0.722	0.0549

ing them to describe the same physical object. We even grant it *twice* the Gaussian budget of our method to account for the fact that we mirror ours splats as well during training. Our method, in contrast, must reconstruct a *single* butterfly whose reflection reproduces the dorsal surface in the direct view and the underside in the mirror *simultaneously and consistently*. Because the held-out views are confined to the dorsal side, the baseline’s duplicated geometry can fit them just as well as our constrained model: on these views there is nothing that enforcing dorsal–ventral consistency improves, so we neither expect nor observe a win for our method on the novel-view metrics. The purpose of Tab. 2 is the opposite—to show that imposing the requirement of reconstructing single, physically consistent object incurs *no meaningful loss* in novel-view-synthesis quality relative to the unconstrained, higher-capacity baseline.

The decisive quality improvement of our method appears only when the camera leaves the training distribution and moves around to the ventral side (Fig. 6). There, the baseline is exposed as two disconnected objects that each describe half of the object accurately, leaving the other side unusable for visualization purposes whereas our reconstruction remains one coherent butterfly that renders correctly from *any* viewpoint.

5. Limitations and Future Work

Residual floaters and foreground isolation. In its effort to explain the background, which for the mirror is a dark surface, 3DGS tends to scatter a halo of *floaters* around the specimen. A simple 3D bounding-box crop (used to render Fig. 1) removes most of them, but some survive and become noticeable against light backgrounds. These floaters are spatially separated from the butterfly, yet cleanly isolating the foreground specimen still requires manual post-processing. We deliberately avoid relying on pixel-perfect segmentation to address this issue, as it tends to struggle with microscopic hairs and antennae. Better isolating the foreground while preserving fine structure with minimal manual input is a promising direction for future work.

Lower fidelity on the ventral surface. The ventral surface is reconstructed at slightly lower fidelity than the dorsal side, because it is seen from fewer viewpoints and only indirectly through the mirror. Capturing additional oblique viewpoints would provide more direct evidence of the ventral surface and help close this gap. The ventral surface also appears slightly darker than in reality, as it was less brightly illuminated than the dorsal side during capture.

6. Conclusion

We have presented a complete acquisition and reconstruction pipeline for high-fidelity novel-view synthesis of mounted butterfly specimens. By combining a non-contact first-surface mirror system, handheld focus stacking with automatic image registration, and a segmentation-free mirror-aware extension of 3D Gaussian Splatting, our system overcomes the challenges encountered when digitizing this class of fragile, detail-rich objects in 3D. The resulting full-surround models will be deployed in a virtual museum experience.

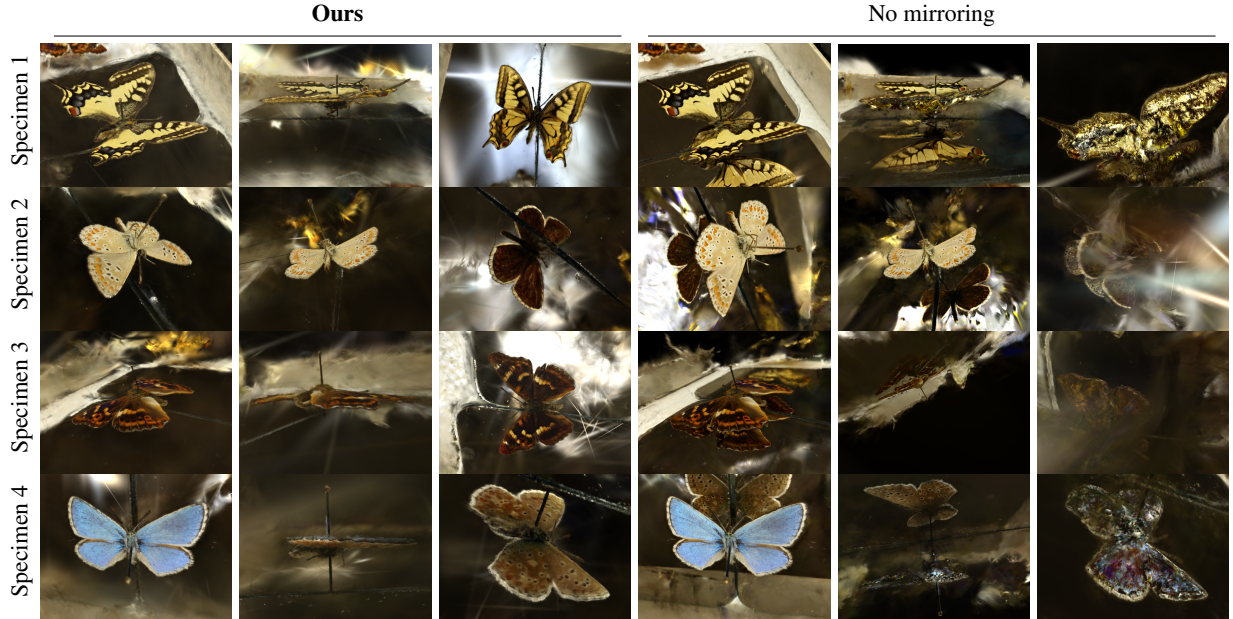


Figure 6. **Qualitative comparison of mirror handling.** For each specimen (row) we show three novel viewpoints per method—roughly dorsal, lateral, and ventral. Our method holds together as a single consistent object, whereas the mirror-unaware baseline disintegrates away from the training views, making the gap clear even where the metrics are close. We deliberately show each method’s *raw, full-scene* render—specimen, mirror, and background—because the foreground is only cropped out in a later step; this unedited output is the fairest comparison, even if it makes the butterfly harder to distinguish from the background by eye. We matched viewpoints across methods where possible, but some baseline poses were so corrupted by floaters that the identical viewpoint rendered nothing legible. There, a representative view is shown instead.

Acknowledgments

We gratefully acknowledge imec IDLab for computational resources via the iLab.t infrastructure.

References

- [1] Abderraouf Amrani, Hamid Laga, Volker Framenau, and Melissa Thomas. Dynamic adaptive sampling for accurate image-based 3d insect reconstruction using neural implicit surfaces. In *2025 International Conference on Digital Image Computing: Techniques and Applications (DICTA)*, pages 1–8. IEEE, 2025. 2
- [2] Peter J. Burt and Edward H. Adelson. A multiresolution spline with application to image mosaics. *ACM Transactions on Graphics*, 2(4):217–236, 1983. 4
- [3] Yang Chen and Gérard Medioni. Object modelling by registration of multiple range images. In *Image and Vision Computing*, pages 145–155, 1992. 4
- [4] Georgios D. Evangelidis and Emmanouil Z. Psarakis. Parametric image alignment using enhanced correlation coefficient maximization. *IEEE Transactions on Pattern Analysis and Machine Intelligence*, 30(10):1858–1865, 2008. 3
- [5] Martin A. Fischler and Robert C. Bolles. Random sample consensus: A paradigm for model fitting with applications to image analysis and automated cartography. In *Communications of the ACM*, pages 381–395, 1981. 4
- [6] Sara Fridovich-Keil et al. Plenoxels: Radiance fields without neural networks. In *Proc. CVPR*, pages 5501–5510, 2022. 2
- [7] Helicon Soft Ltd. Helicon focus. <https://www.heliconsoft.com/heliconsoft-products/helicon-focus/>, 2026. Version 8.4
- [8] Bernhard Kerbl, Georgios Kopanas, Thomas Leimkühler, and George Drettakis. 3D Gaussian Splatting for Real-Time Radiance Field Rendering. *ACM Transactions on Graphics*, 42(4):1–14, 2023. 2, 4, 5
- [9] Hengjia Li and Chuong Nguyen. Perspective-consistent multifocus multiview 3d reconstruction of small objects. In *2019 Digital Image Computing: Techniques and Applications (DICTA)*, pages 1–8. IEEE, 2019. 2
- [10] Jiayue Liu, Xiao Tang, Freeman Cheng, Roy Yang, Zhihao Li, Jianzhuang Liu, Yi Huang, Jiaqi Lin, Shiyong Liu, Xiaofei Wu, et al. Mirrorgaussian: Reflecting 3d gaussians for reconstructing mirror reflections. In *European Conference on Computer Vision*, pages 377–393. Springer, 2024. 3
- [11] Li Ma, Xiaoyu Li, Jing Liao, Qi Zhang, Xuan Wang, Jue Wang, and Pedro V Sander. Deblur-nerf: Neural radiance fields from blurry images. In *Proceedings of the IEEE/CVF conference on computer vision and pattern recognition*, pages 12861–12870, 2022. 2
- [12] Jiarui Meng, Haijie Li, Yanmin Wu, Qiankun Gao, Shuzhou Yang, Jian Zhang, and Siwei Ma. Mirror-3dgs: Incorporating

- mirror reflections into 3d gaussian splatting. *arXiv preprint arXiv:2404.01168*, 2024. 3
- [13] Ben Mildenhall, Pratul P. Srinivasan, Matthew Tancik, Jonathan T. Barron, Ravi Ramamoorthi, and Ren Ng. NeRF: Representing Scenes as Neural Radiance Fields for View Synthesis. In *European Conference on Computer Vision (ECCV)*, 2020. 2
- [14] Thomas Müller et al. Instant neural graphics primitives with a multiresolution hash encoding. *ACM Trans. Graph.*, 41(4): 102:1–102:15, 2022. 2
- [15] Shree K. Nayar and Yasuo Nakagawa. Shape from focus. *IEEE Transactions on Pattern Analysis and Machine Intelligence*, 16(8):824–831, 1994. 2
- [16] Gil Nelson and Deborah L Paul. Dissco, idigbio and the future of global collaboration. *Biodiversity Information Science and Standards*, 2019. 1
- [17] Chuong V Nguyen, David R Lovell, Matt Adcock, and John La Salle. Capturing natural-colour 3d models of insects for species discovery and diagnostics. *PLoS one*, 9(4):e94346, 2014. 2
- [18] Fabian Plum and David Labonte. scant—an open-source platform for the creation of 3d models of arthropods (and other small objects). *PeerJ*, 9:e11155, 2021. 2
- [19] Radu Bogdan Rusu, Nico Blodow, and Michael Beetz. Fast point feature histograms (FPFH) for 3D registration. In *IEEE International Conference on Robotics and Automation (ICRA)*, pages 3212–3217, 2009. 4
- [20] Paul-Edouard Sarlin, Cesar Cadena, Roland Siegwart, and Marcin Dymczyk. From coarse to fine: Robust hierarchical localization at large scale. In *IEEE Conference on Computer Vision and Pattern Recognition (CVPR)*, 2019. 3
- [21] Paul-Edouard Sarlin, Daniel DeTone, Tomasz Malisiewicz, and Andrew Rabinovich. Superglue: Learning feature matching with graph neural networks. In *Proceedings of the IEEE/CVF conference on computer vision and pattern recognition*, pages 4938–4947, 2020. 3
- [22] Johannes L. Schönberger and Jan-Michael Frahm. Structure-from-Motion Revisited. In *IEEE Conference on Computer Vision and Pattern Recognition (CVPR)*, pages 4104–4113, 2016. 3
- [23] Liao Shen, Tianqi Liu, Huiqiang Sun, Jiaqi Li, Zhiguo Cao, Wei Li, and Chen Change Loy. Dof-gaussian: Controllable depth-of-field for 3d gaussian splatting. In *Proceedings of the Computer Vision and Pattern Recognition Conference*, pages 26462–26471, 2025. 2
- [24] Vincent Stuart Smith, Kristina Gorman, Wouter Addink, Christos Arvanitidis, Ana Casino, Katherine Dixey, Gabriele Dröge, Quentin Groom, Elspeth Margaret Haston, Donald Hobern, et al. Synthesis+ abridged grant proposal. *Research Ideas and Outcomes*, 5:e46404, 2019. 1
- [25] Bernhard Ströbel, Sebastian Schmelzle, Nico Blüthgen, and Michael Heethoff. An automated device for the digitization and 3d modelling of insects, combining extended-depth-of-field and all-side multi-view imaging. *ZooKeys*, (759):1, 2018. 2
- [26] LichtFeld Studio. Lichtfeld studio, 2026. 5
- [27] Yujie Wang, Praneeth Chakravarthula, and Baoquan Chen. Dof-gs: Adjustable depth-of-field 3d gaussian splatting for post-capture refocusing, defocus rendering and blur removal. *arXiv preprint arXiv:2405.17351*, 2024. 2, 6, 7
- [28] Zhou Wang, Alan C. Bovik, Hamid R. Sheikh, and Eero P. Simoncelli. Image quality assessment: From error visibility to structural similarity. *IEEE Transactions on Image Processing*, 13(4):600–612, 2004. 6
- [29] Chang Xu, Jiayuan Liu, Chuong Nguyen, Fabien Casten, Benoit Maujean, and Simone Gasparini. 3d reconstruction of insects: an improved multifocus stacking and an evaluation of learning-based mvs approaches. In *2021 International Conference on 3D Vision (3DV)*, pages 1411–1419. IEEE, 2021. 2
- [30] Richard Zhang, Phillip Isola, Alexei A. Efros, Eli Shechtman, and Oliver Wang. The unreasonable effectiveness of deep features as a perceptual metric. In *IEEE Conference on Computer Vision and Pattern Recognition (CVPR)*, 2018. 6